https://ntrs.nasa.gov/search.jsp?R=19910005245 2020-03-19T19:29:44+00:00Z

IN-34-CR
319 995
P.25

COMPUTATION OF THERMOCHEMICAL NONEQUILIBRIUM FLOWS AROUND A SIMPLE AND A DOUBLE ELLIPSE

Tahir Gökçen

Eloret Institute, 3788 Fabian Way, Palo Alto, California 94303
Work performed at NASA Ames Research Center, Moffett Field, CA 94035
under Cooperative Agreement NCC2-420

I. INTRODUCTION

The nonequilibrium viscous reactive flows over a simple and a double ellipse at 30° angle of attack have been computed. The geometry and the free stream conditions are given by INRIA/GAMNI/SMAI workshop test cases 6.2-2 and 6.2-4.[1] The governing Navier-Stokes equations coupled with thermochemical nonequilibrium processes are solved numerically using a fully coupled, implicit, finite volume technique with a dynamically adaptive grid. The nonequilibrium gas model and the numerical method used in the calculations will be briefly described in the following sections, while the details can be found in Refs. 2-3.

II. FORMULATION

1. Nonequilibrium Gas Model For Air

The present nonequilibrium gas model for air consists of the following five chemical species: three diatomic species, molecular nitrogen N_2, molecular oxygen O_2, nitric oxide NO; and two atomic species, nitrogen N and oxygen O.

Since the diatomic species have internal structure, excitations of the internal degrees of freedom, vibrational and rotational, are considered as thermal nonequilibrium processes. It is assumed that the local thermodynamic equilibrium within each class of degrees of freedom is maintained.[4,5] These classes are assumed to be the class of translational degrees of freedom for all species and the classes of vibrational and rotational degrees of freedom for the diatomic species. As a result of the assumed thermal equilibrium within each class, the local thermodynamic state of the gas can be described by three temperatures corresponding to each energy mode, i. e., translational temperature T, vibrational temperature T_v, and rotational temperature T_r. Equilibrium between these three energy modes is assumed to be governed by rate processes.

The implicit assumption in this three temperature model is that the equilibration time scale for each class of the internal mode is small compared to the flow time scale. As a result, each internal energy mode is distributed to its equilibrium distribution instantaneously, and can be described by a temperature.

2. Governing Equations

The governing equations are basically the continuum Navier-Stokes equations of gas dynamics. They are augmented to account for the nonequilibrium processes and are briefly presented herein. As a result of the nonequilibrium processes considered, six additional partial differential equations are added to the conventional Navier-Stokes equations. The equation of conservation of mass is replaced by five species equations due to the chemical

(NASA-CR-187702) COMPUTATION OF THERMOCHEMICAL NONEQUILIBRIUM FLOWS AROUND A SIMPLE AND A DOUBLE ELLIPSE (Eloret Corp.) 25 p CSCL 20D
N91-14558
Unclas
G3/34 0319995

nonequilibrium, and two additional energy conservation equations are considered for the vibrational and the rotational energy due to the thermal nonequilibrium.

For simplicity the governing equations are presented in Cartesian tensor notation. The species continuity equation, which states the conservation of mass for species i in the gas mixture, is given by

$$\frac{\partial \rho_i}{\partial t} + \frac{\partial}{\partial x_k}(\rho_i u_k + j_{ik}) = w_i, \tag{1}$$

and the familiar mass-averaged momentum equation, which states the conservation of momentum for the gas mixture, is

$$\frac{\partial \rho u_j}{\partial t} + \frac{\partial}{\partial x_k}(\rho u_j u_k + \tau_{jk} + p\,\delta_{jk}) = 0. \tag{2}$$

Two additional energy equations are introduced to account for the thermal nonequilibrium processes, i. e., the relaxation of vibrational and rotational degrees of freedom. Hence, the conservation of vibrational energy within diatomic species is expressed by

$$\frac{\partial E_v}{\partial t} + \frac{\partial}{\partial x_k}(u_k E_v + q_{vk}) = w_v, \tag{3}$$

and similarly, the conservation of rotational energy is

$$\frac{\partial E_r}{\partial t} + \frac{\partial}{\partial x_k}(u_k E_r + q_{rk}) = w_r. \tag{4}$$

Finally, the conservation of total energy is stated by

$$\frac{\partial E}{\partial t} + \frac{\partial}{\partial x_k}[u_k (E + p) + q_k + u_j \tau_{jk}] = 0. \tag{5}$$

The equation of state or pressure of the gas mixture is given by the Dalton's Law of Partial Pressures,

$$p = \sum_{i=1}^{ns} p_i = \rho \bar{R} T. \tag{6}$$

The total energy per unit volume, E, is made up of the various modes of internal energy, i. e., translational, vibrational and rotational modes, the kinetic energy of the flow, and the energy arising from the formation of species. These terms, written in the order mentioned, give the following expression for the total energy

$$E = \rho \bar{C}_v T + E_v + E_r + \frac{1}{2}\rho (u^2 + v^2) + \sum_{i=1}^{ns} \rho_i h_i^o. \tag{7}$$

For the diatomic species: the vibrational energy is calculated assuming a harmonic oscillator model with a cut off energy level corresponding to the dissociation energy (*truncated harmonic oscillator*)[6,7]; and the rotational energy is calculated assuming a rigid

dumbell model. The vibrational and rotational energies in diatomic species i are then expressed by

$$E_{vi} = \rho_i \frac{\hat{R}}{M_i}\left(\frac{\theta_{vi}}{e^{\theta_{vi}/T_v} - 1} - \frac{\theta_{di}}{e^{\theta_{di}/T_v} - 1}\right),$$
$$E_{ri} = \rho_i \frac{\hat{R}}{M_i} T_r, \tag{8}$$

and the total vibrational and rotational energy in the gas is the sum of the energies in the diatomic species.

Since the source terms associated with the chemical nonequilibrium processes are well known (e.g., see Park.[9-11]), it will not be repeated here. The rate constants for chemical reactions are taken from Park.[9] Similarly, in the vibrational and rotational energy equations, Eqs. (3) and (4), the source terms w_v and w_r involve several collisional energy exchange mechanisms.[3,8-11]

The source term in the vibrational energy equation for molecular species i is given by

$$w_{vi} = \frac{E^*_{vi} - E_{vi}}{\tau_{vi}} - w_{fi}\,\bar{E}_i(T, T_v) + w_{bi}\,\bar{G}_i(T). \tag{9}$$

The first term on the right hand side of Eq. (9) represents the rate of vibration-translation energy exchange for the Landau-Teller model of the harmonic oscillator. Other terms are due to the vibration-dissociation coupling (see Ref. 6-7). In the vibration-dissociation model, $\bar{E}_i(T, T_v)$ is the average energy lost from vibration to a single dissociation and $\bar{G}_i(T)$ is the average energy gained from a recombination. The expressions for $\bar{E}_i(T, T_v)$ and $\bar{G}_i(T)$ are taken from Marrone and Treanor.[7]

The source term in the rotational energy equation is similar to the term in the vibrational energy equation. In the present work, only the rotation-translation exchange mechanism,

$$w_{ri} = \frac{E^*_{ri} - E_{ri}}{\tau_{ri}}, \tag{10}$$

is considered.

The diffusive fluxes are assumed to be *linearly* related to the gradients of the associated flow quantities. The Navier-Stokes diffusion of momentum relates the shear stress tensor to the velocity gradient tensor, i. e., the Newtonian fluid assumption; Fourier's law of heat conduction relates the heat flux vector to the associated temperature gradient; and Fick's law of diffusion relates the diffusive mass fluxes to gradients of species concentration.

For the viscosity of species i the following expression is used:

$$\ln \mu_i = (A_i \ln T + B_i) \ln T + C_i. \tag{11}$$

The coefficients A_i, B_i, and C_i for species i are taken from Moss[12]. The thermal conductivity of translational energy for species i is calculated using

$$\kappa_i = \frac{5}{2}\mu_i\, c_{v_{ti}}. \tag{12}$$

Once the viscosity and thermal conductivity of each chemical species are specified, the viscosity and thermal conductivity of the gas mixture are computed using the semiempirical *Wilke's mixture rule.*[13] The thermal conductivities of vibrational and rotational energies, analogous to Eucken relation, are calculated by

$$\begin{aligned} \kappa_v &= \sum_{i=1}^{nm} c_{v_{vi}}\, \mu_i, \\ \kappa_r &= \sum_{i=1}^{nm} c_{v_{ri}}\, \mu_i. \end{aligned} \tag{13}$$

The diffusion coefficient $\mathcal{D}$ is specified assuming constant Schmidt number for all species,

$$Sc = \frac{\mu}{\rho\,\mathcal{D}} = 0.5. \tag{14}$$

The vibrational and rotational relaxation times are specified such that the collision numbers of the vibrational and rotational relaxation, Z_v and Z_r, are 50 and 5, respectively. The mean collision time is estimated using the mean free path λ and the mean speed $\bar{c}$

$$\tau_{coll.} = \frac{\lambda}{\bar{c}}, \tag{15}$$

and the vibrational and rotational relaxation times are then calculated by

$$\begin{aligned} \tau_v &= Z_v\, \tau_{coll.} = 50\, \tau_{coll}, \\ \tau_r &= Z_r\, \tau_{coll.} = 5\, \tau_{coll}. \end{aligned} \tag{16}$$

The above specifications are made such that the present nonequilibrium air model is compatible with the five species DSMC air model of Moss *et al.*[14]

III. METHODOLOGY

1. Numerical Method

The numerical method is based on that presented by MacCormack[15] for solving the two dimensional perfect gas Navier-Stokes equations. This method has the following useful features: it is implicit, which allows one to take large time steps to reach the steady state solution; it uses a flux vector splitting similar to that of Steger and Warming[16] to mimic convective transport and/or to maintain numerical stability; and it uses the Gauss-Seidel Line Relaxation technique with the block tridiagonal matrix inversion. Candler and MacCormack[17–19] applied this method to solve the two dimensional Navier-Stokes equations with thermochemical nonequilibrium processes. In the present work, the method is extended to include a shock capturing technique with dynamically adaptive grids.

2. Adaptive Grid Algorithm

The adaptive grid strategy used here follows the work presented by Eiseman[20] and Abolhassani *et al.*[21] Grid motion is established directly in one physical dimension (normal to the wall) using a weight function in such a way that the weight function and some

measure of the mesh size would be held approximately constant for the grid. Large values of the weight cause small mesh spacing and produce the desired clustering of the points while small values of the weight produce the opposite effect, i.e., large mesh spacing. The useful form of the weight function is given by the linear combination[20]

$$w = 1 + \sum_{k=1}^{m} C_k M_k. \tag{17}$$

As to the choice of the weight functions M_k, the gradients of the flow variables seem to be a natural choice. This choice produces good results as long as the chosen flow variable is monotonic in the direction that the grid is being adapted. Otherwise, a simple gradient produces coarse mesh spacing where the chosen flow variable has an extremum. This disadvantage can be avoided by incorporating the second derivative into the weight function. In the present work, five functions for M_k are used. These are the gradients of the pressure, tangential velocity, species mass fraction, temperature, and kinetic energy of the flow. These functions proved to be satisfactory for a wide range of flow conditions.

IV. RESULTS

The results presented here are for the viscous reactive flows over a simple and a double ellipse at 30° angle of attack. The simple/double ellipse geometry is provided by INRIA/GAMNI/SMAI workshop test cases 6.2.[1] For all calculations, a freestream Mach number $M_\infty = 25$, unit Reynolds number $Re_\infty/\text{m} = 2.2 \times 10^4$, and temperature and pressure of 75 km standard atmosphere ($T = 205.3°K$ and $p = 2.52$ Pa) are prescribed. The wall is assumed to be at $1500°K$ and noncatalytic to chemical reactions.

The adaptive grid used for the simple ellipse case (test case 6.2-2) is depicted in Fig. 1. As seen from Fig. 1, the grid around the ellipse is adapted to the flow gradients of the bow shock wave and the viscous boundary layer near the wall. In Figs. 2-8, the flowfield over the ellipse is represented in terms of contour plots. Fig. 2 shows the Mach number contours. It should be mentioned that the Mach number is based on the frozen speed of sound. Since the rotational degrees of freedom are treated to be nonequilibrium with the translational degrees in the gas, the speed of sound is larger than that of one (or two) temperature models in which translational and rotational degrees are assumed to be in equilibrium. Therefore, the computed Mach number is lower than that of one (or two) temperature models. In Figs. 3-5, translational, rotational and vibrational temperature fields are shown, respectively. It appears, from Figs. 3 and 4, that the translational and rotational temperature fields are identical. For the flow conditions prescribed in this test, the rotational relaxation occurs very fast behind the shock wave. In fact, everywhere in the flowfield, except for a few points right behind the shock, the rotational temperature is in equilibrium with the translational temperature. This justifies the assumption that one temperature can characterize translational and rotational modes of the internal energy at low altitudes. However, for more rarefied cases this assumption breaks down, and the rotational relaxation needs to be considered. As far as the vibrational relaxation is concerned, a close examination of Fig. 4 and 5 shows that the vibrational temperature in most of the flowfield is different from the translational temperature. The previous temperature figures show the extent of thermal nonequilibrium in the flowfield. Figs. 6

and 7 show the extent of chemistry in the flowfield in terms of atomic nitrogen and atomic oxygen mass fraction contours. Fig. 6 shows that considerable amount of N is produced due to dissociation of N_2 near the nose region and on the compression (windward) side of ellipse and to a smaller extent on the expansion (leeward) side. It is observed from Fig. 7 that almost all O_2 is dissociated right behind the shock wave and recombined in the cool boundary layer on the compression side.

Most of the comments made on the simple ellipse calculations equally apply to the double ellipse calculations. Fig. 8 shows the grid used for the double ellipse calculations. Again, the converged grid is adapted to the flow gradients of the bow shock wave and the viscous boundary layer near the wall. The computed flowfield around the double ellipse is represented by the contour plots Figs. 9-13, and the surface quantities Figs. 14-18. Fig. 9 shows the pressure coefficient contours. Although the detached bow shock wave is obvious from the contours, the canopy shock is not observed because of the increment used in the contours of C_p. Figs. 10-11 represents the translational and vibrational temperature contours and the extent of thermal nonequilibrium in the flow, and Figs. 12-13 give the contours of atomic nitrogen and oxygen. The surface quantities, the pressure coefficient C_p, the skin friction coefficient C_f and the Stanton number St, are shown in Figs. 14-16, respectively. Finally, distributions of atomic species N and O at the wall are shown in Figs. 17 and 18.

V. CONCLUDING REMARKS

The thermochemical nonequilibrium viscous flows are solved numerically using a fully coupled, implicit, finite volume technique with a dynamically adaptive grid. The adaptive grid is necessary because there are regions of the flowfield where a predetermined grid fails to resolve the flow characteristics such as near shock waves and the viscous boundary layer.

The present air model includes thermal as well as chemical nonequilibrium effects. It is shown that most of the flowfield is in vibrational nonequilibrium, which may show significant differences with respect to flow chemistry compared to one temperature model suggested in the workshop problem. However, it is clear that for the computed test cases the rotational relaxation is not important.

References

1. *Workshop on Hypersonic Flows for Reentry Problems*, INRIA/GAMNI/SMAI, Brochure of December 1988.
2. Gökçen, T., and MacCormack, R. W., "Nonequilibrium Effects for Hypersonic Transitional Flows Using Continuum Approach," *AIAA paper 89-0461*, 1989.
3. Gökçen, T., "Computation of Hypersonic Low Density Flows with Thermochemical Nonequilibrium," *Ph. D Thesis*, Stanford University, 1989.
4. Wood, W. W., and Kirkwood, G. J., "Hydrodynamics of a Reacting and Relaxing Fluid," *Journal of Applied Physics*, Vol. 28, No. 4, 1957, pp. 395-398. Also, *Shock and Detonation Waves*, edited by W. W. Wood, *Documents on Modern Physics*, 1967, pp. 112-119.
5. Clarke, J. F. and McChesney, M., *Dynamics of Relaxing Gas* , Butterworth Publishers, London and Boston, 1976.

6. Treanor, C. E., and Marrone, P. V., "Effect of Dissociation on the Rate of Vibrational Relaxation," *Physics of Fluids*, Vol. 5, No. 9, 1962, pp. 1022-1026.
7. Marrone, P. V., and Treanor, C. E., "Chemical Relaxation with Preferential Dissociation from Excited Vibrational Levels," *Physics of Fluids*, Vol. 6, No. 9, 1963, pp. 1215-1221.
8. Lambert, T. D., *Vibrational and Rotational Relaxation in Gases*, Clarendon Press, Oxford, 1977.
9. Park, C. "On Convergence of Chemical Reacting Flows," *AIAA paper 85-0247*, 1985.
10. Park, C. " Modern Developments in Chemical Reacting Flows," *AA 222 Class Notes*, Stanford University, 1988.
11. Park, C., *Nonequilibrium Hypersonic Aerothermodynamics*, John Wiley and Sons, New York, 1989.
12. Moss, J. N., Private Communications.
13. Wilke, C. R., "A Viscosity Equation for Gas Mixtures," *Journal of Chemical Physics*, Vol. 18, No. 4, April 1950, pp. 517.
14. Moss, J. N., Bird, G. A., and Dogra, K. V., "Nonequilibrium Thermal Radiation for an Aeroassist Flight Experiment Vehicle," *AIAA paper 88-0081*, 1988.
15. MacCormack, R. W., "Current Status of the Numerical Solutions of the Navier-Stokes Equations," *AIAA paper 85-0032*, 1985.
16. Steger, J., and Warming, R. F., "Flux Vector Splitting of the Inviscid Gas Dynamics Equations with Applications to Finite Difference Methods," *NASA TM-78605*, 1979.
17. Candler, G. V., and MacCormack, R. W., "The Computation of Hypersonic Flows in Chemical and Thermal Nonequilibrium," Presented at the *Third National Aero-Space Plane Technology Symposium*, NASA-Ames, Moffett Field, CA June 2-4 1987.
18. Candler, G. V., and MacCormack, R. W., "The Computation of Hypersonic Ionized Flows in Chemical and Thermal Nonequilibrium," *AIAA paper 88-0511*, 1988.
19. Candler, G. V., "The Computation of Weakly Ionized Hypersonic Flows in Thermo-Chemical Nonequilibrium," *Ph. D Thesis*, Stanford University, 1988.
20. Eiseman, R. P., "Grid Generation For Fluid Mechanics Computations," *Annual Review of Fluid Mechanics*, Vol. 17, 1985, pp. 487-522, edited by Van Dyke, M., Vincenti, W. G., Wehausen, J. V.
21. Abolhassani, S. J., Smith, R. E., Tiwari, S. N, "Grid Adaption For Hypersonic Flow," *AIAA CP 87-1169*, 1987.

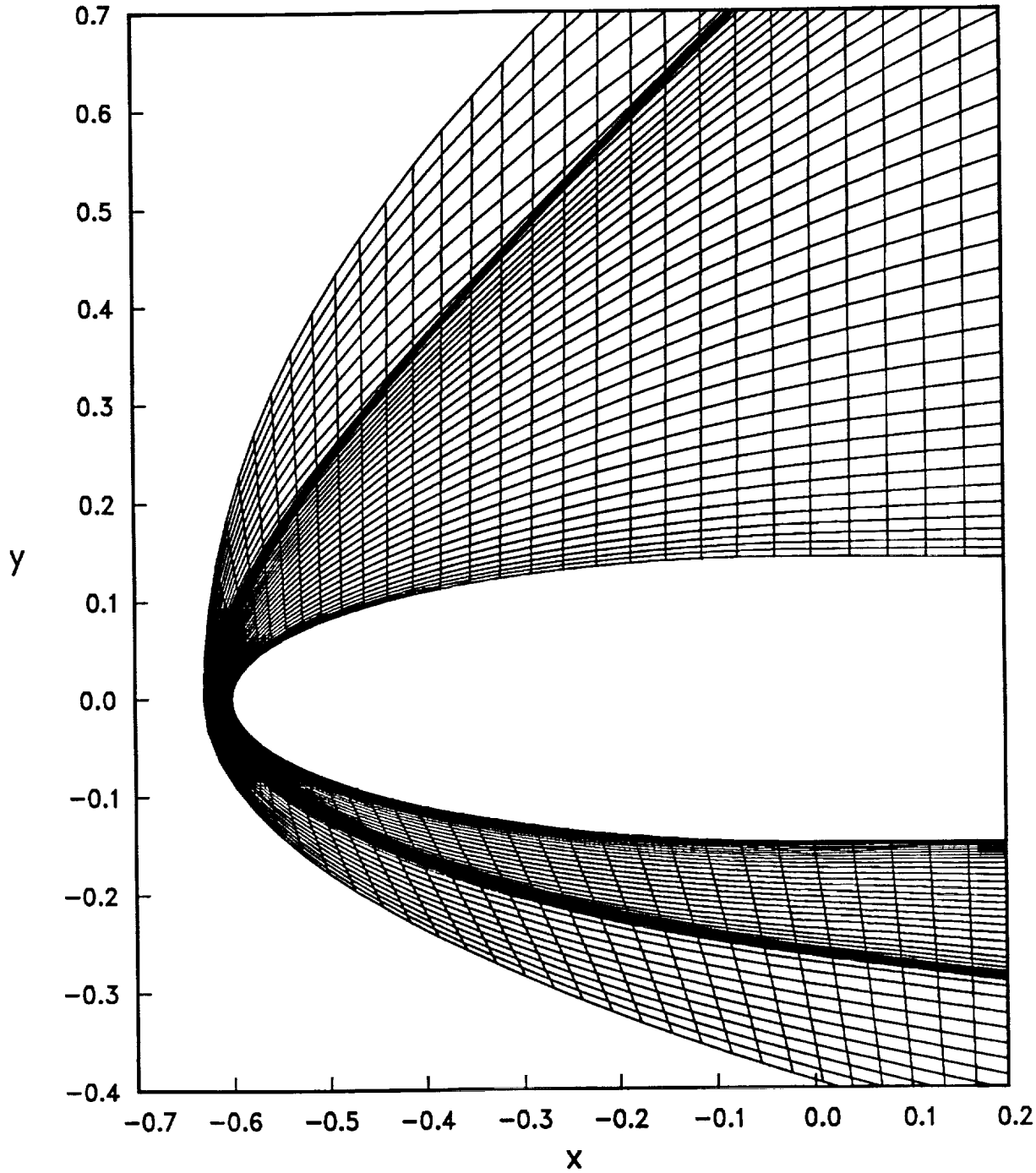

Fig. 1. Adaptive grid for reactive flow over a simple ellipse (60×45).
Test Case 6. 2-2: $\alpha = 30°$, $M_\infty = 25$, $Re_\infty/\mathrm{m} = 2.2 \times 10^4$

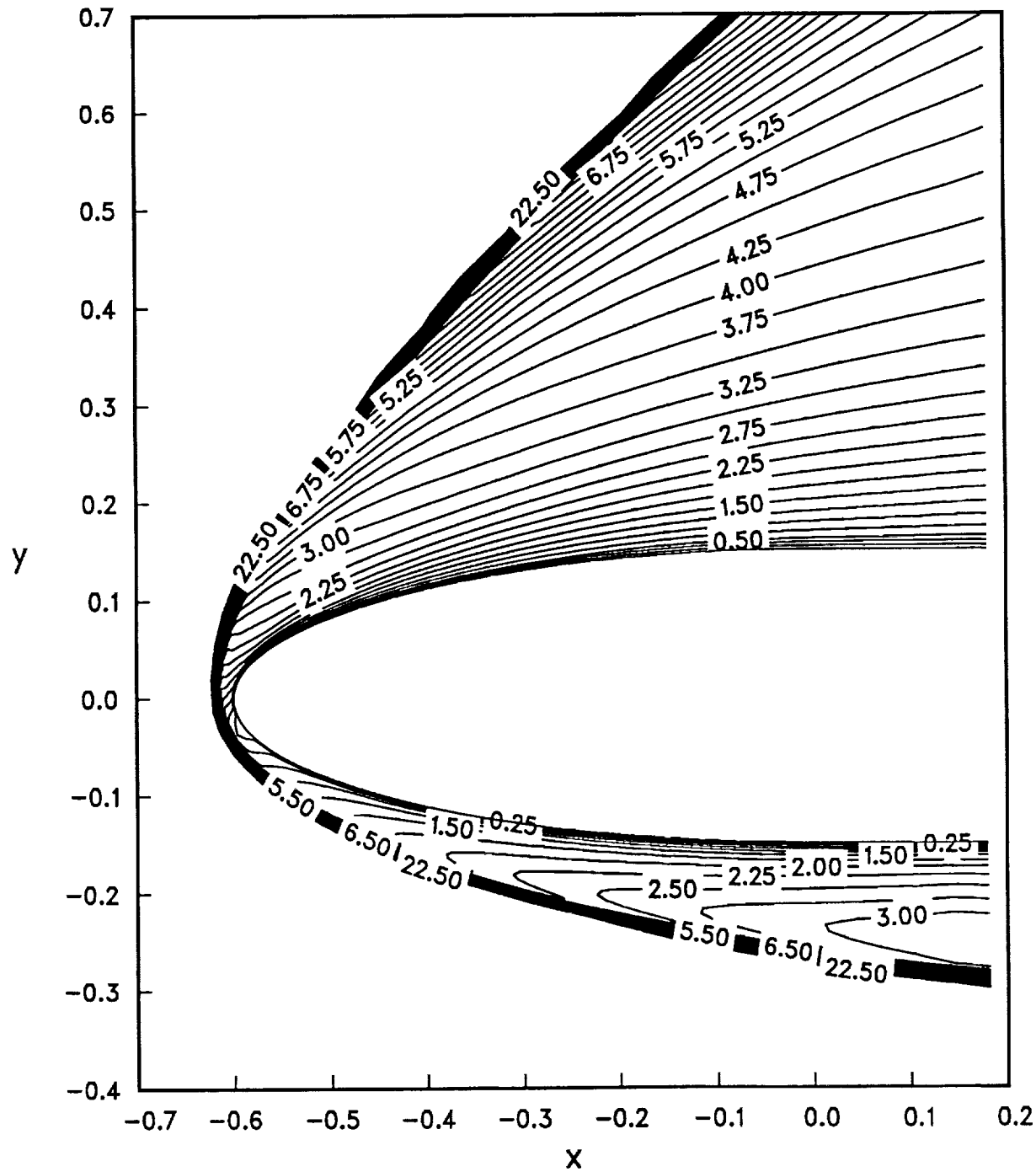

Fig. 2. Mach number contours over a simple ellipse.
Test Case 6. 2-2: $\alpha = 30°$, $M_\infty = 25$, $Re_\infty/\mathrm{m} = 2.2 \times 10^4$

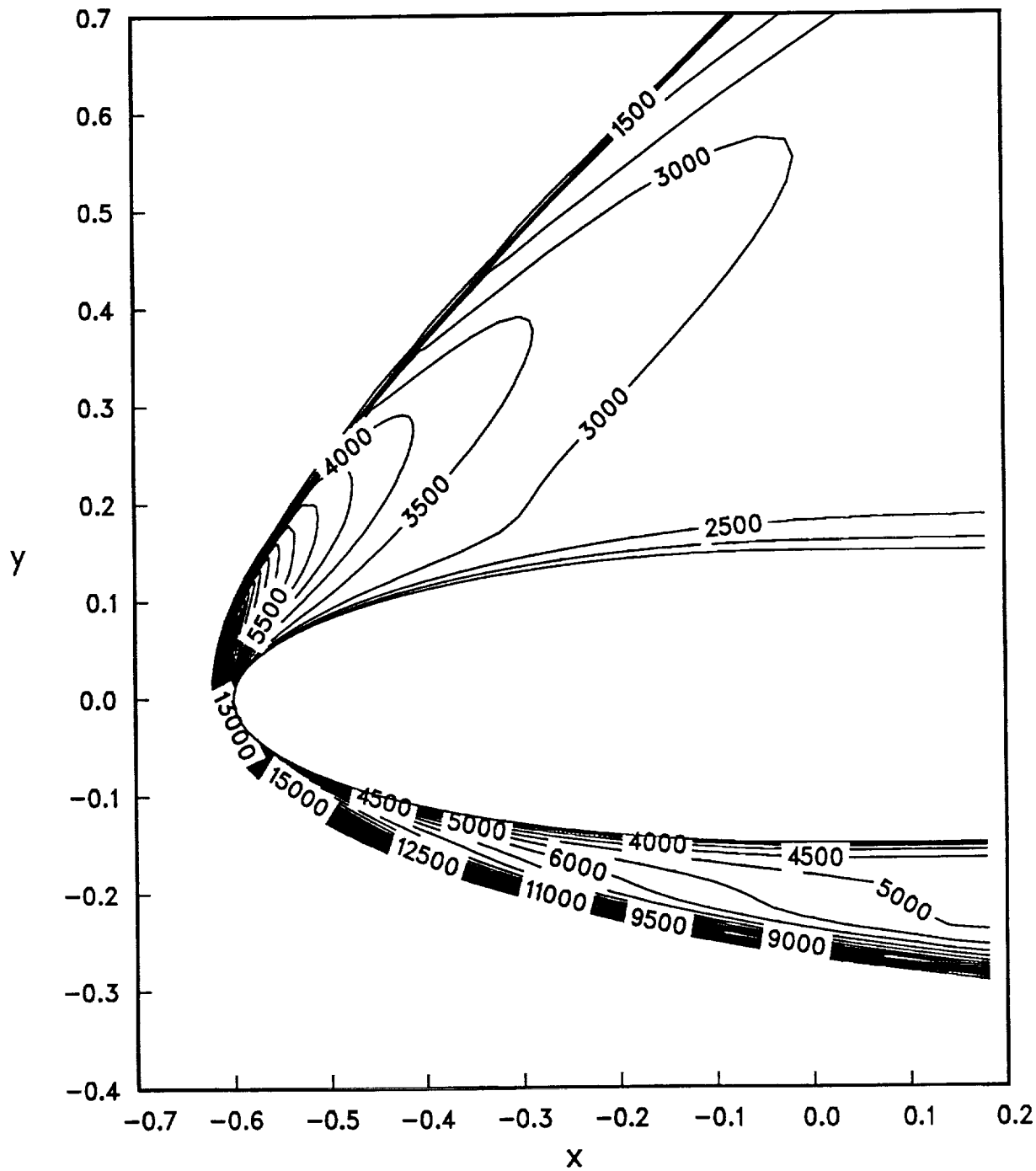

Fig. 3. Translational temperature contours over a simple ellipse.
Test Case 6. 2-2: $\alpha = 30°$, $M_\infty = 25$, $Re_\infty/\mathrm{m} = 2.2 \times 10^4$

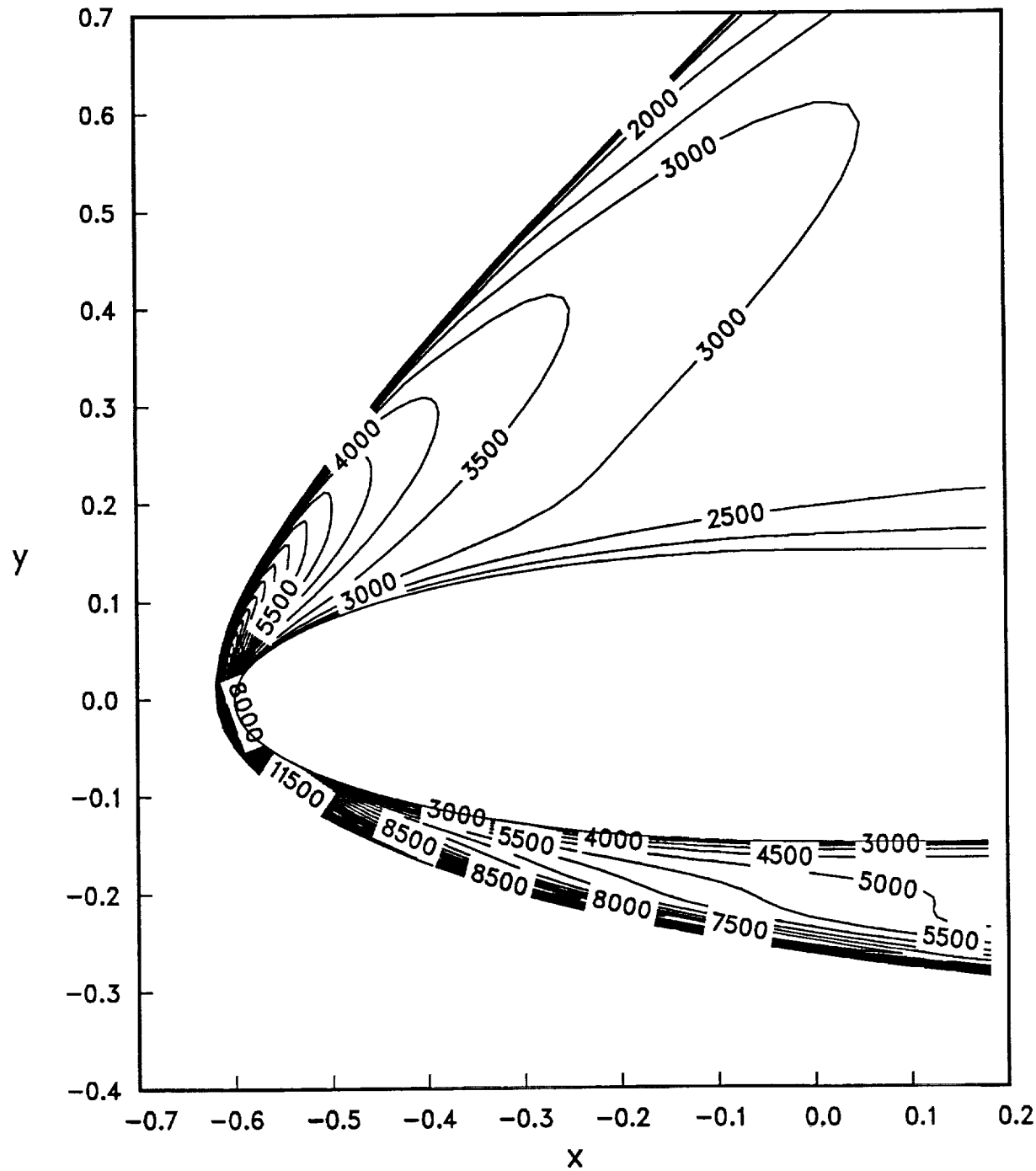

Fig. 4. Rotational temperature contours over a simple ellipse.
Test Case 6. 2-2: $\alpha = 30°$, $M_\infty = 25$, $Re_\infty/\mathrm{m} = 2.2 \times 10^4$

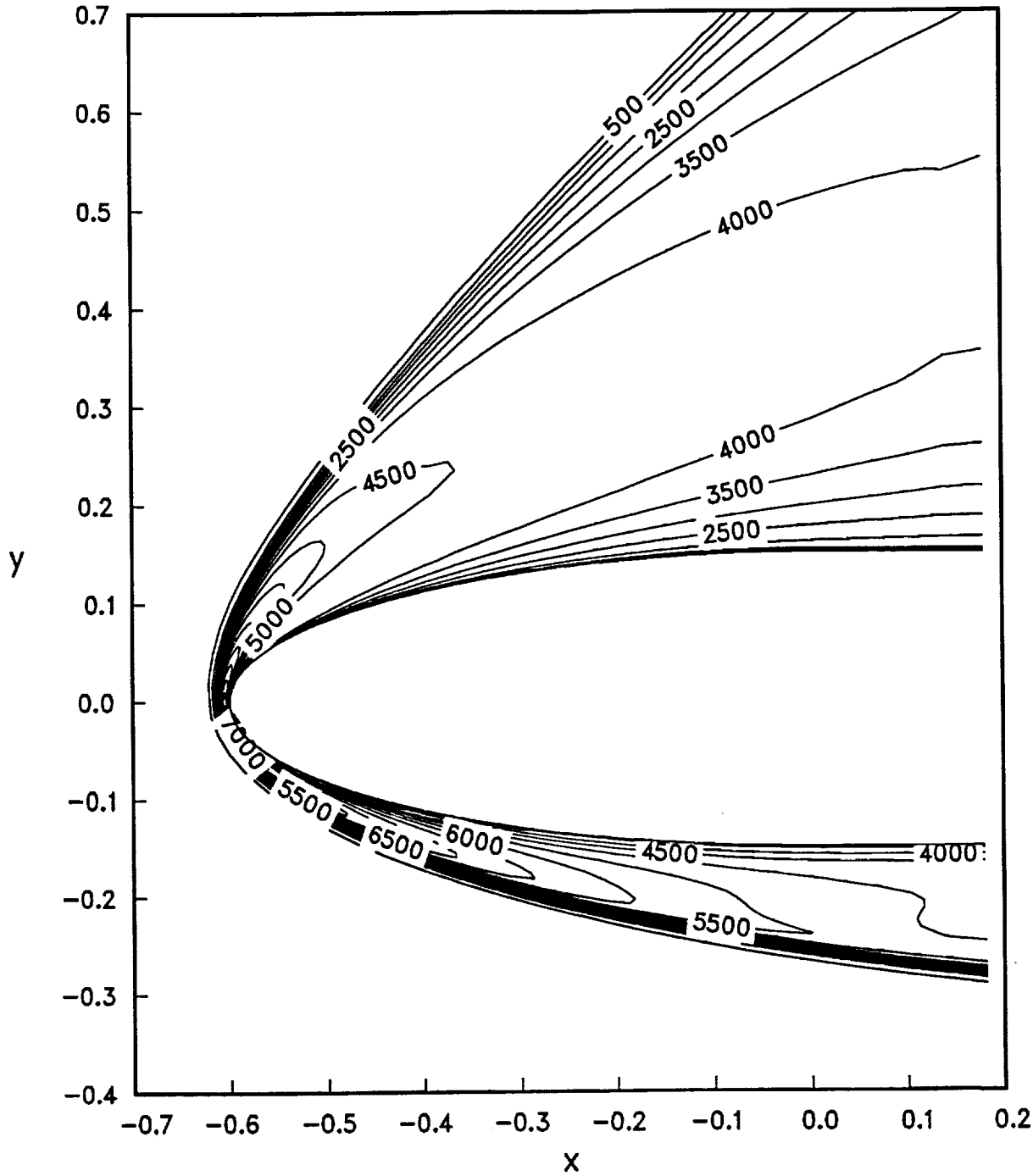

Fig. 5. Vibrational temperature contours over a simple ellipse.
Test Case 6.2-2: $\alpha = 30°$, $M_\infty = 25$, $Re_\infty/\mathrm{m} = 2.2 \times 10^4$

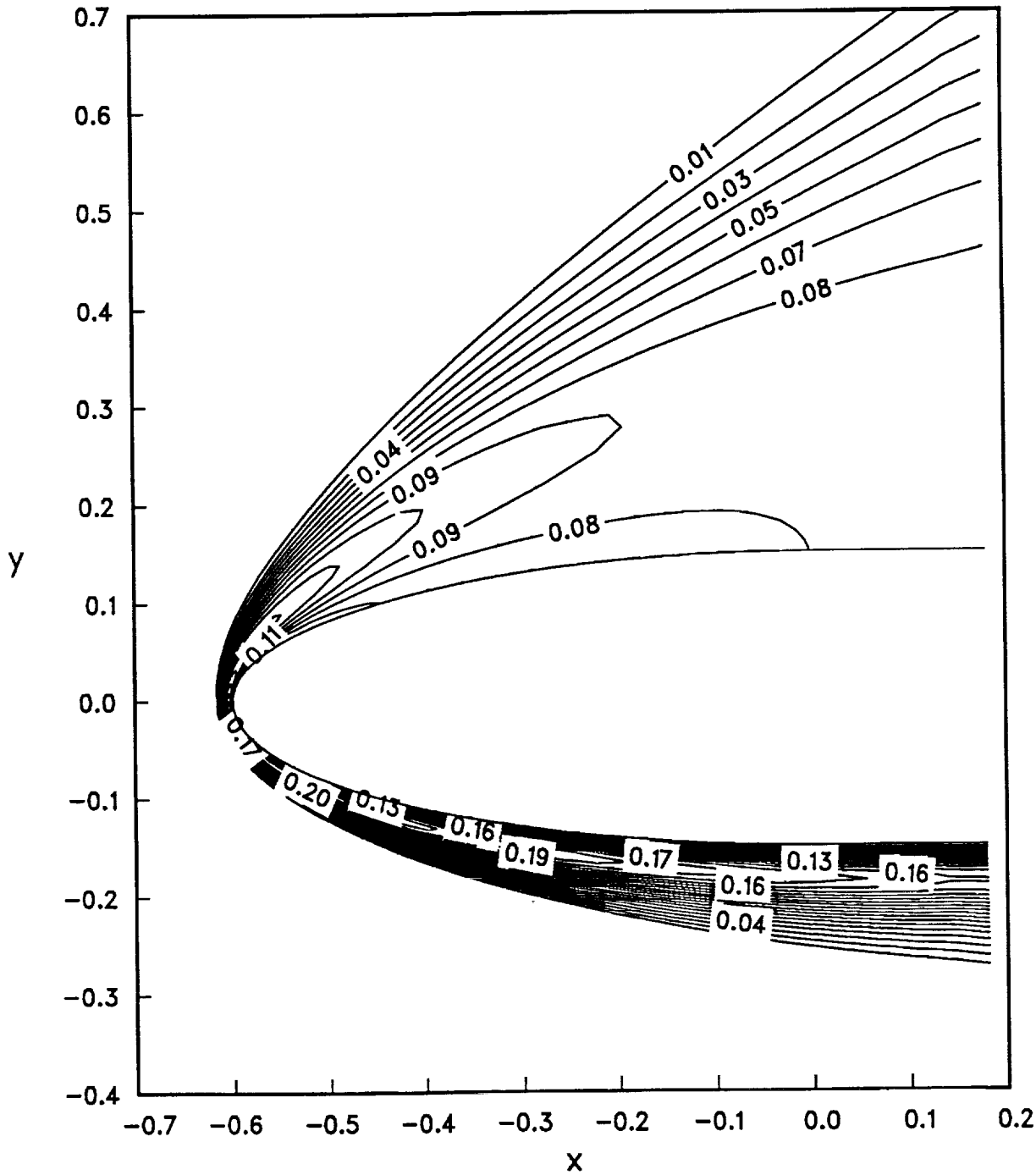

Fig. 6. Atomic nitrogen N contours over a simple ellipse.
Test Case 6. 2-2: $\alpha = 30°$, $M_\infty = 25$, $Re_\infty/\mathrm{m} = 2.2 \times 10^4$

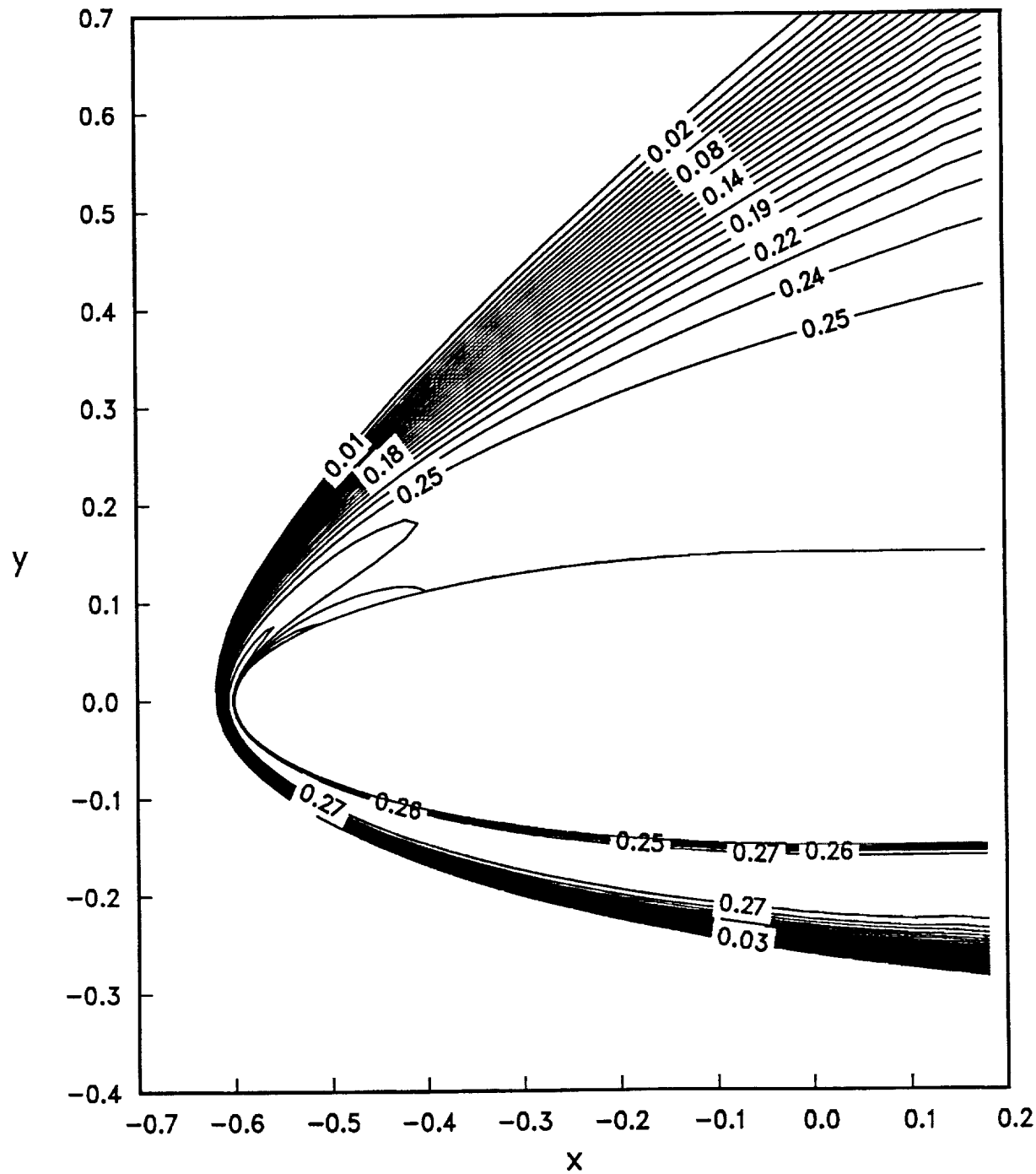

Fig. 7. Atomic oxygen O contours over a simple ellipse.
Test Case 6. 2-2: $\alpha = 30°$, $M_\infty = 25$, $Re_\infty/\mathrm{m} = 2.2 \times 10^4$

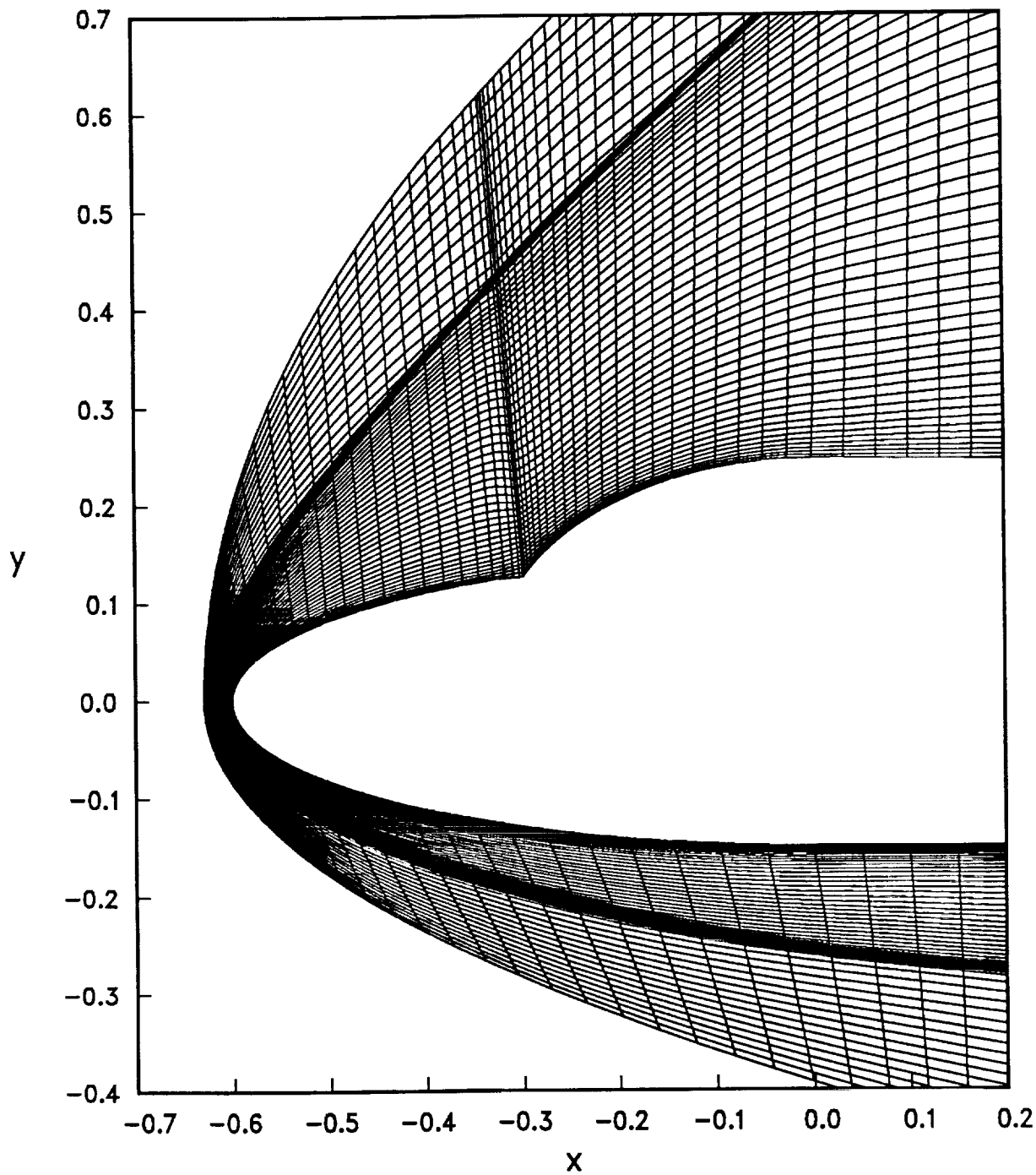

Fig. 8. Adaptive grid for reactive flow over a double ellipse (90×60). Test Case 6. 2-4: $\alpha = 30°$, $M_\infty = 25$, $Re_\infty/\mathrm{m} = 2.2 \times 10^4$

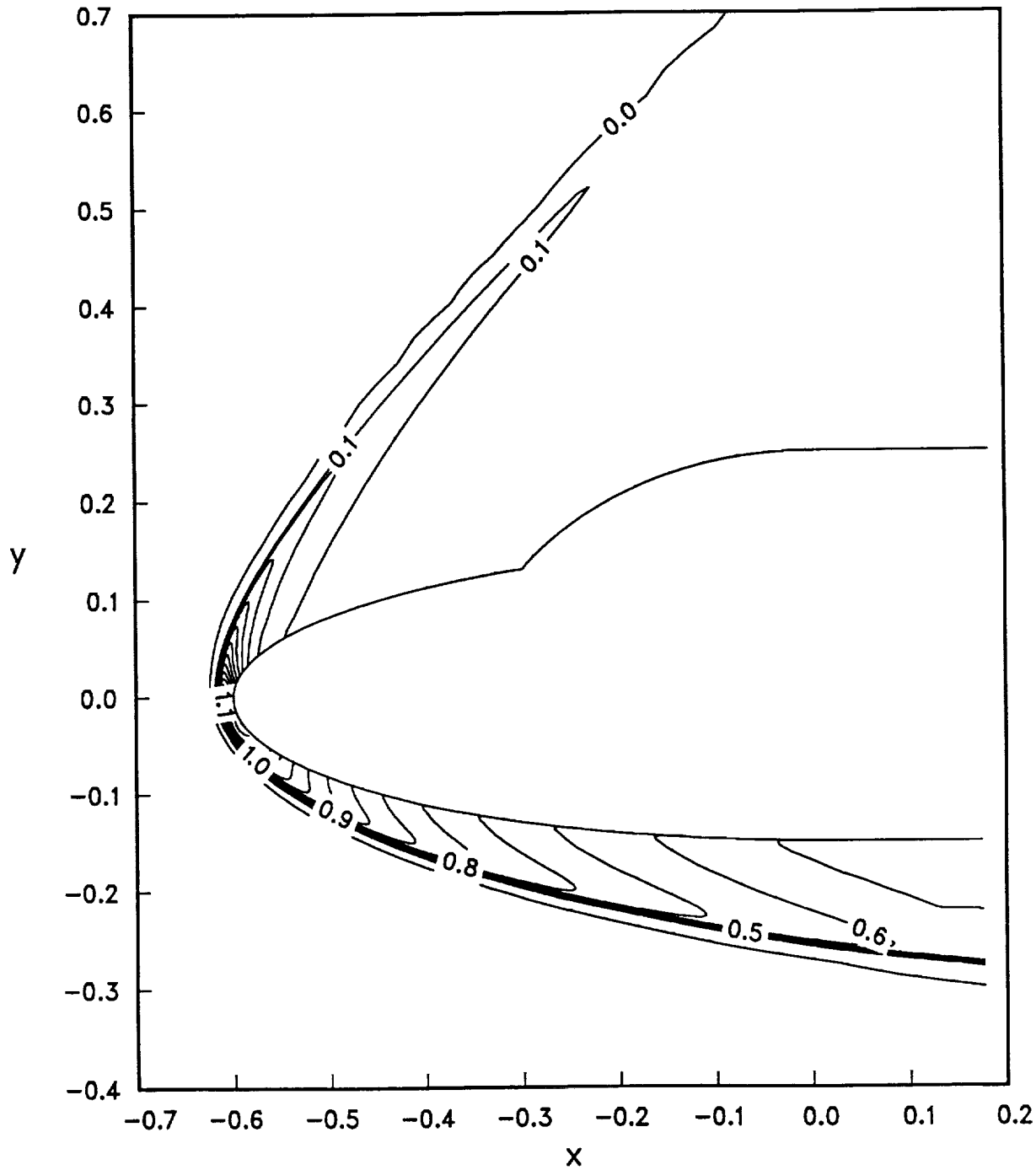

Fig. 9. Pressure coefficient contours over a double ellipse.
Test Case 6. 2-4: $\alpha = 30°$, $M_\infty = 25$, $Re_\infty/\mathrm{m} = 2.2 \times 10^4$

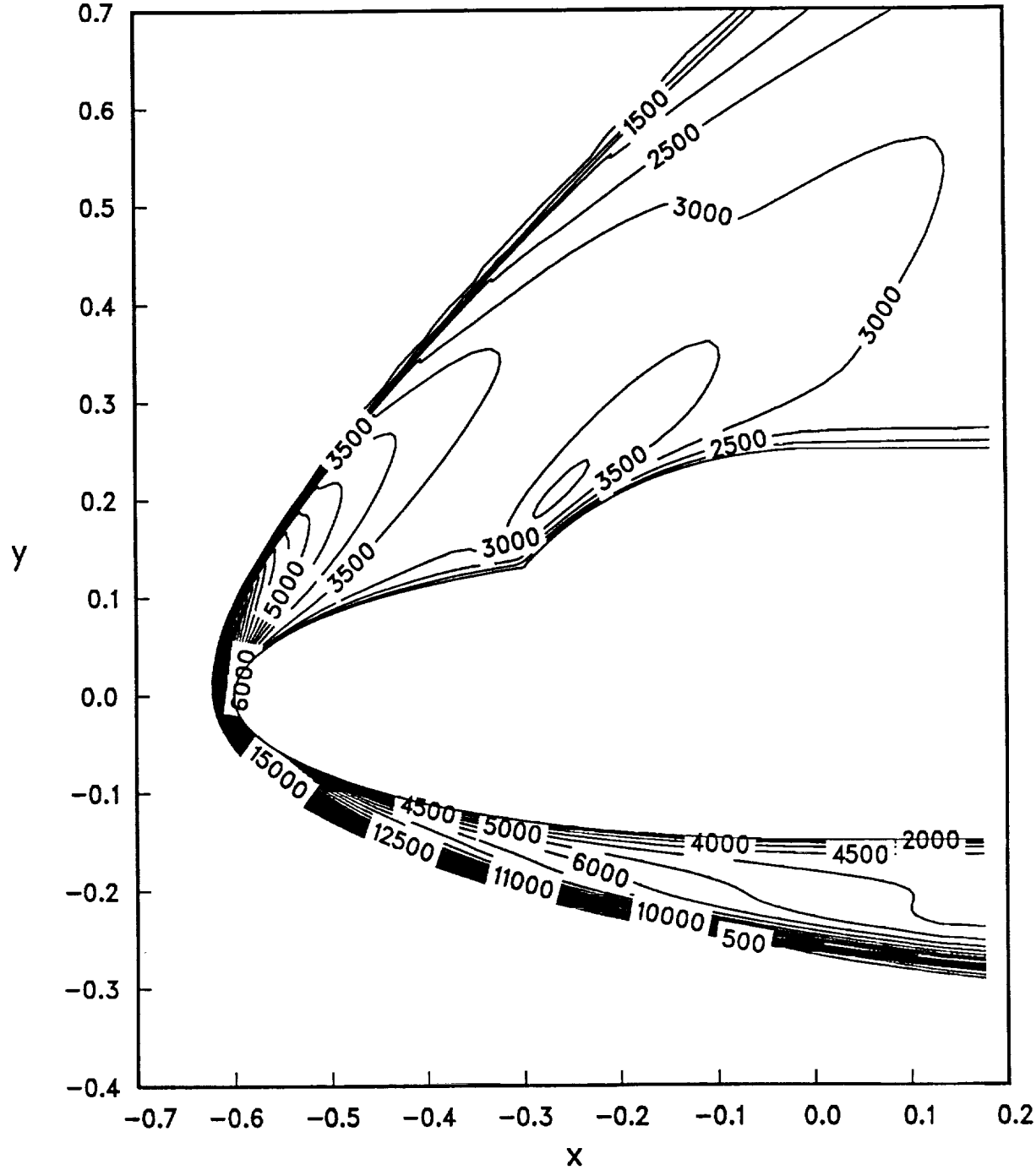

Fig. 10. Translational temperature contours over a double ellipse.
Test Case 6. 2-4: $\alpha = 30°$, $M_\infty = 25$, $Re_\infty/\mathrm{m} = 2.2 \times 10^4$

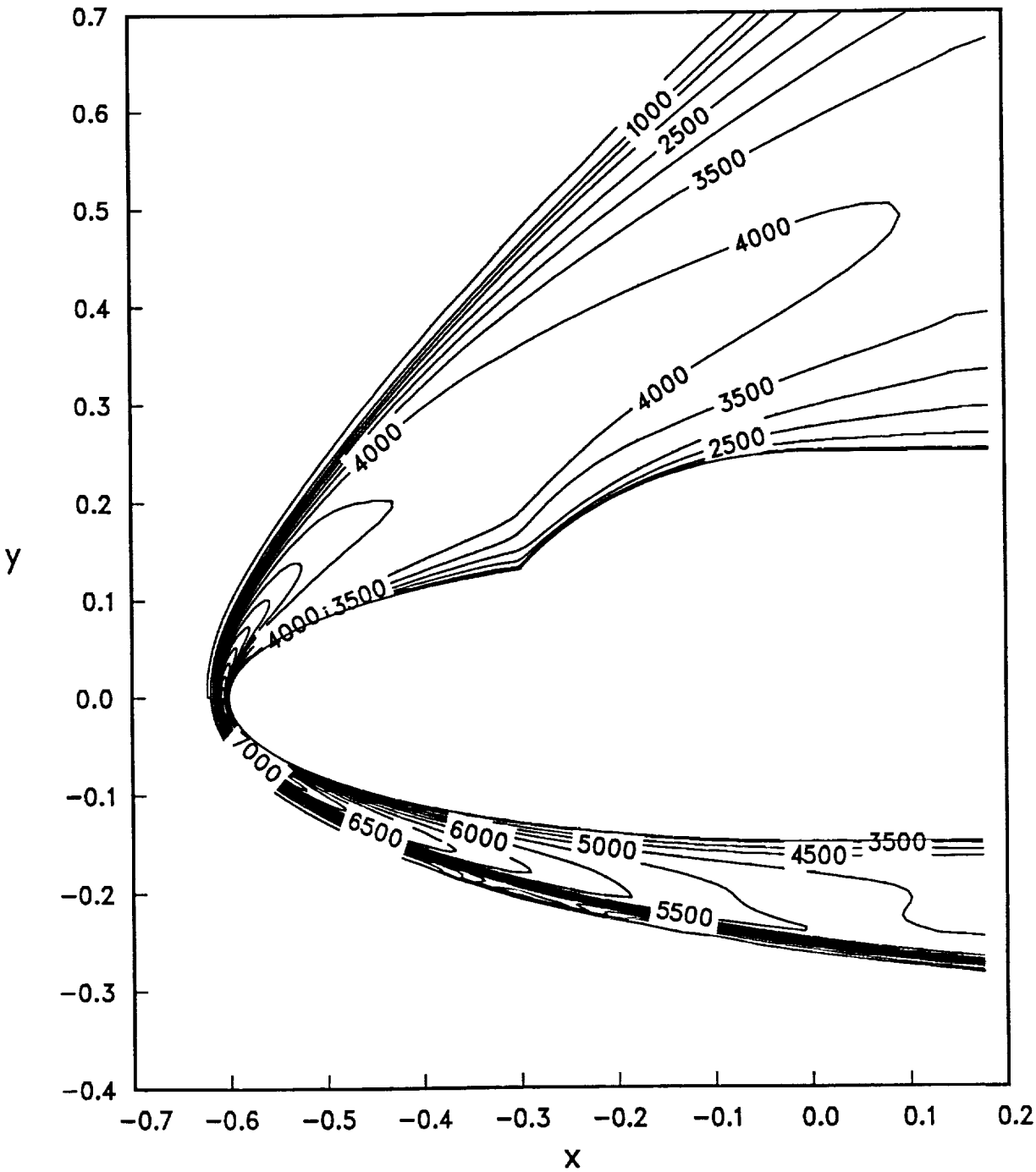

Fig. 11. Vibrational temperature contours over a double ellipse.
Test Case 6. 2-4: $\alpha = 30°$, $M_\infty = 25$, $Re_\infty/\mathrm{m} = 2.2 \times 10^4$

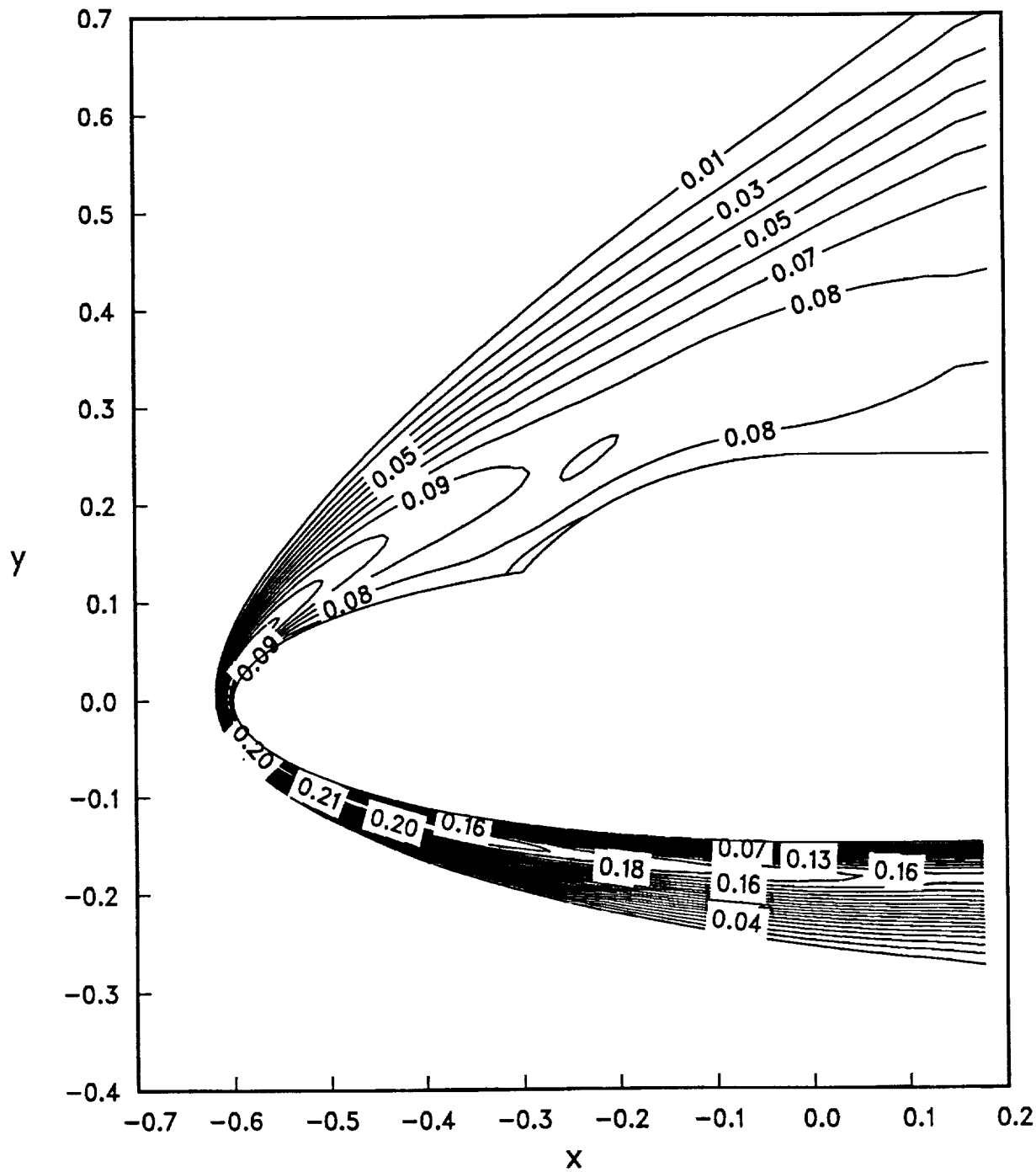

Fig. 12. Atomic nitrogen N contours over a double ellipse.
Test Case 6. 2-4: $\alpha = 30°$, $M_\infty = 25$, $Re_\infty/\mathrm{m} = 2.2 \times 10^4$

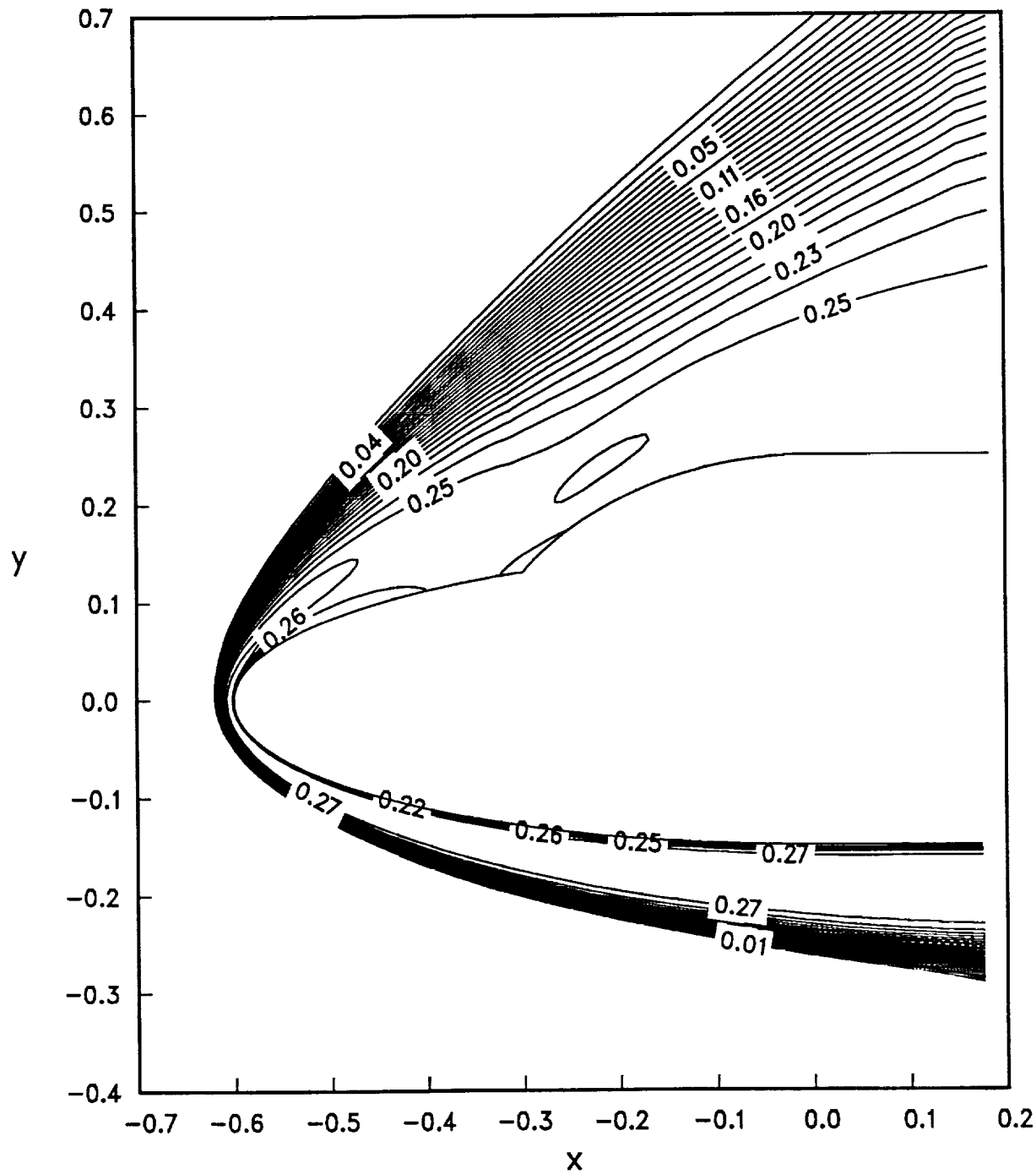

Fig. 13. Atomic oxygen O contours over a double ellipse.
Test Case 6. 2-4: $\alpha = 30°$, $M_\infty = 25$, $Re_\infty/\mathrm{m} = 2.2 \times 10^4$

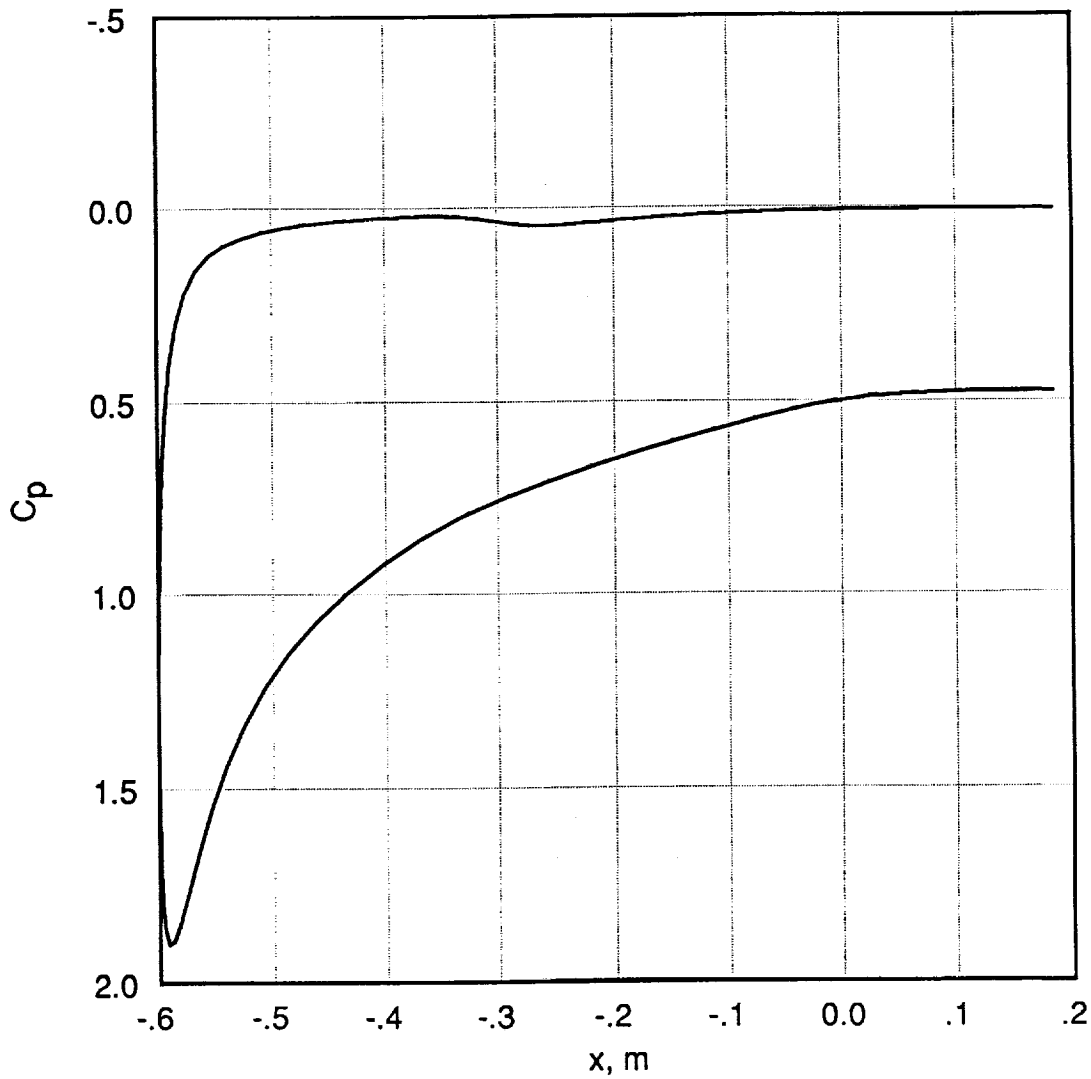

Fig. 14. Distribution of pressure coefficient at the wall of the double ellipse. Test Case 6. 2-4: $\alpha = 30°$, $M_\infty = 25$, $Re_\infty/\mathrm{m} = 2.2 \times 10^4$

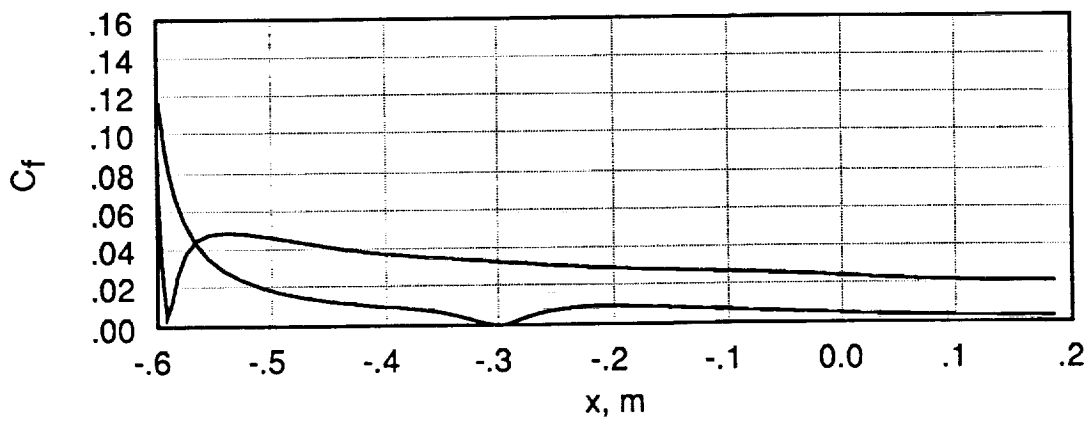

Fig. 15. Distribution of skin friction coefficient for the double ellipse. Test Case 6. 2-4: $\alpha = 30°$, $M_\infty = 25$, $Re_\infty/\mathrm{m} = 2.2 \times 10^4$

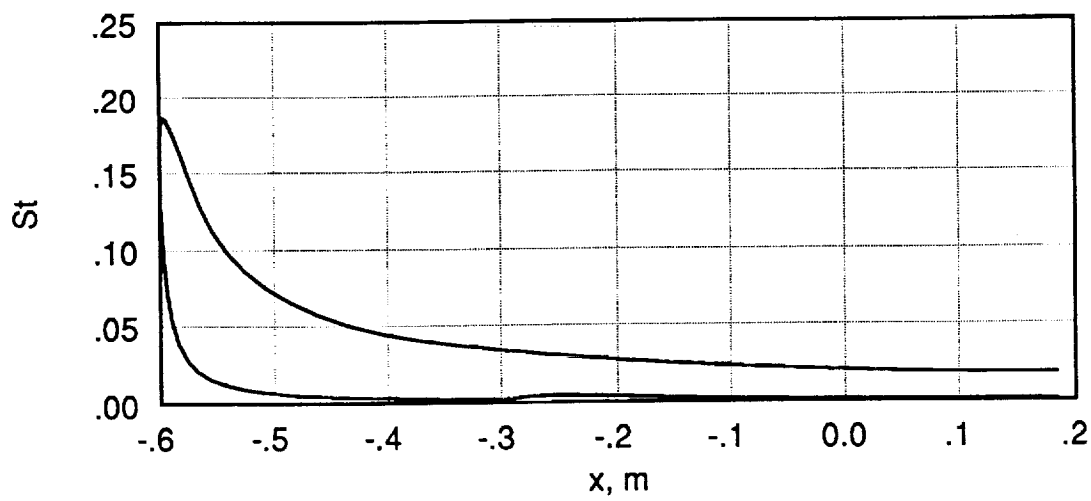

Fig. 16. Distribution of Stanton number at the wall of the double ellipse. Test Case 6. 2-4: $\alpha = 30°$, $M_\infty = 25$, $Re_\infty/\mathrm{m} = 2.2 \times 10^4$

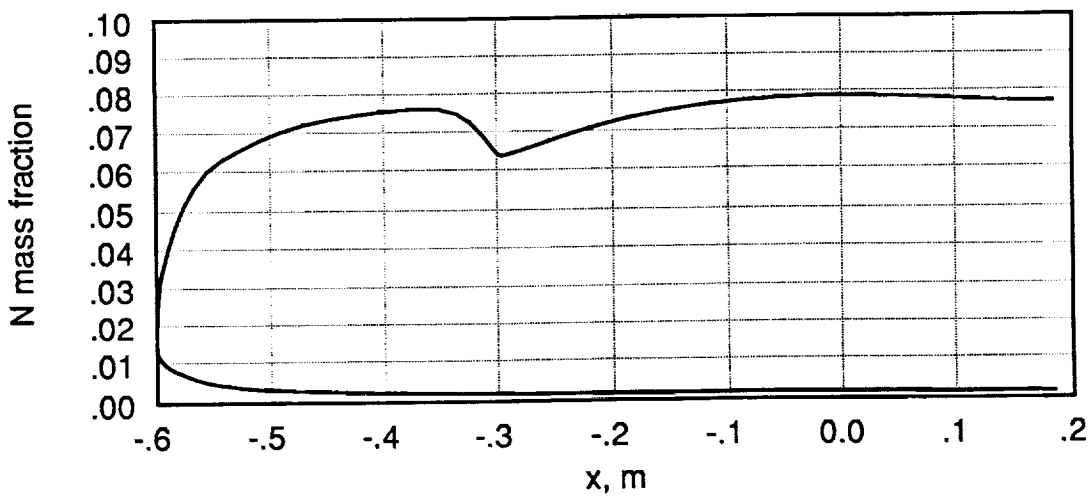

Fig. 17. Distribution of N mass fraction at the wall of the double ellipse. Test Case 6. 2-4: $\alpha = 30°$, $M_\infty = 25$, $Re_\infty/\mathrm{m} = 2.2 \times 10^4$

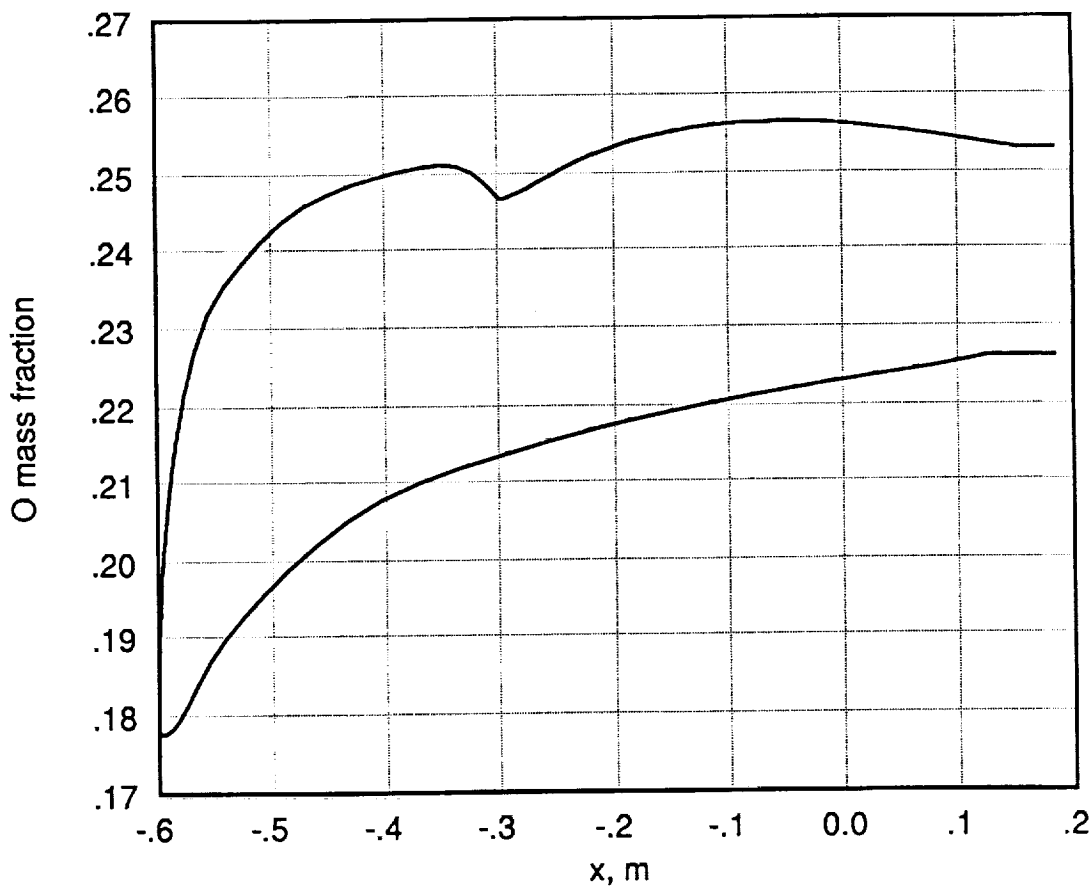

Fig. 18. Distribution of O mass fraction at the wall of the double ellipse. Test Case 6. 2-4: $\alpha = 30°$, $M_\infty = 25$, $Re_\infty/\mathrm{m} = 2.2 \times 10^4$